

Feature Pyramid Network with Multi-Head Attention for Semantic Segmentation of Fine-Resolution Remotely Sensed Images

Rui Li ¹, Shunyi Zheng ¹, and Chenxi Duan ^{2,*}

¹ School of Remote Sensing and Information Engineering, Wuhan University, Wuhan 430079, China

² State Key Laboratory of Information Engineering in Surveying, Mapping, and Remote Sensing, Wuhan University, 430079, China

* Correspondence: chenxiduan@whu.edu.cn (C. Duan)

Abstract: Semantic segmentation from fine-resolution remotely sensed images is an urgent issue in satellite imagery processing. Due to the complicated environment, automatic categorization and segmentation is a challenging matter especially for images with a fine resolution. Solving it can help to surmount a wide varied range of obstacles in urban planning, environmental protection, and natural landscape monitoring, which paves the way for complete scene understanding. However, the existing frequently-used encoder-decoder structure is unable to effectively combine the extracted spatial and contextual features. Therefore, in this paper, we introduce the Feature Pyramid Network (FPN) to bridge the gap between the low-level and high-level features. Moreover, we enhance the contextual information with the elaborate Multi-Head Attention module and propose the Feature Pyramid Network with Multi-Head Attention (FPN-MHA) for semantic segmentation of fine-resolution remotely sensed images. Extensive experiments conducted on the ISPRS Potsdam and Vaihingen datasets demonstrate the effectiveness of our FPN-MHA. Code is available at <https://github.com/lironui/FPN-MHA>.

Keywords: semantic segmentation; deep learning; attention mechanism

1. Introduction

Semantic segmentation of remotely sensed images (i.e., assigns each pixel in images with a definite land cover category) has become one of the most crucial leverages for ground object interpretation [1], which plays a crucial role in urban planning, environmental protection, and natural landscape monitoring [2-4]. Meanwhile, land cover information can also provide insights from a panoramic perspective to tackle a multitude of socioeconomic and environmental challenges, such as food insecurity, poverty, climate change, and disaster risk. With recent advances in Earth observation technology, a constellation of satellite and airborne platforms have been launched [5,6]. Therefore, substantial fine-resolution remotely sensed images are available now for semantic segmentation. Traditionally, to manifest the physical properties of land cover, vegetation indices are frequently-used measures for extracting features from multi-spectral/multi-temporal images. However, the adaptability and flexibility of these indices are severely restricted by their high dependency on hand-crafted descriptors [7,8].

With the rise of the convolutional neural network (CNN), plenty of dramatic breakthroughs of semantic segmentation have been experienced in recent years. Compared to vegetation indices that merely take finite bands into account, CNN can employ a wide variety of information, such as periods, spectrums, and the interactions between different categories of land cover. Besides, the powerful ability to capture nonlinear and hierarchical features automatically enables CNN to do not rely on hand-crafted descriptors, which makes the end-to-end framework possible.

Fully Convolutional Network (FCN) [9] is the first proven and effective end-to-end CNN structure. Restricted by the oversimple design of the decoder, the results of FCN, although very encouraging, appear coarse. Subsequently, the more elaborate encoder-decoder structure [10,11] is proposed which comprises two symmetric paths: a contracting path for extracting features and an expanding path for exact positioning to accomplish more accurate results. Also, the dilated or atrous convolution [12,13] has shown its powerful capability for enlarging receptive fields without shrinking spatial resolution. Therefore, several following networks for semantic segmentation are proposed based on the encoder-decoder framework [10,14,15] or dilation backbone [16-18]. For segmentation, the thorough extraction of the global contextual information and multiscale semantic features with varying sizes are fairly vital for accuracy. Therefore, a series of researches hammer at this issue.

The pyramid scene parsing network (PSPNet) [19] aggregates contextual information among different regions via the elaborate spatial pyramid pooling module. DeeplabV3 [20] adopts atrous convolution to mining multiscale features, which is employed as the decoder module in DeepLabV3+ [21] to further improve the segmentation performance. The dual attention network (DANet) [22] designs the attention model with two branches (i.e., the spatial attention module and the channel attention module) based on the dot-product attention mechanism to extract abundant contextual relationships. However, restricted by the enormous memory and computational consumptions which increase quadratically with the input size, DANet simply attaches the dot-product attention mechanism at the lowest layer and merely captures the long-range dependencies from the smallest feature maps.

As the time and space complexity is the bottleneck that crucially hinders the applicability and practicability, many subsequent studies aim to lower the complexity of the dot-product attention mechanism. The utilization of sparse factorizations reduces the complexity of attention from $O(N^2)$ to $O(N\sqrt{N})$ [23], while the usage of locality-sensitive hashing further reduces the complexity to $O(N \log N)$ [24]. Thereafter, taking the attention mechanism as a dot-product of kernel feature maps, Katharopoulos et al. [25] and Li et al. [15] go the extra miles and linearize the module. The advanced recent developments have immensely expanded the possibilities of the attention mechanism, which greatly enhances the ability of encoder-decoder structures to capture context information extraction. However, the lack of capacity to completely combine the extracted spatial and contextual features still constraints the potential of encoder-decoder structures which has not been efficiently solved.

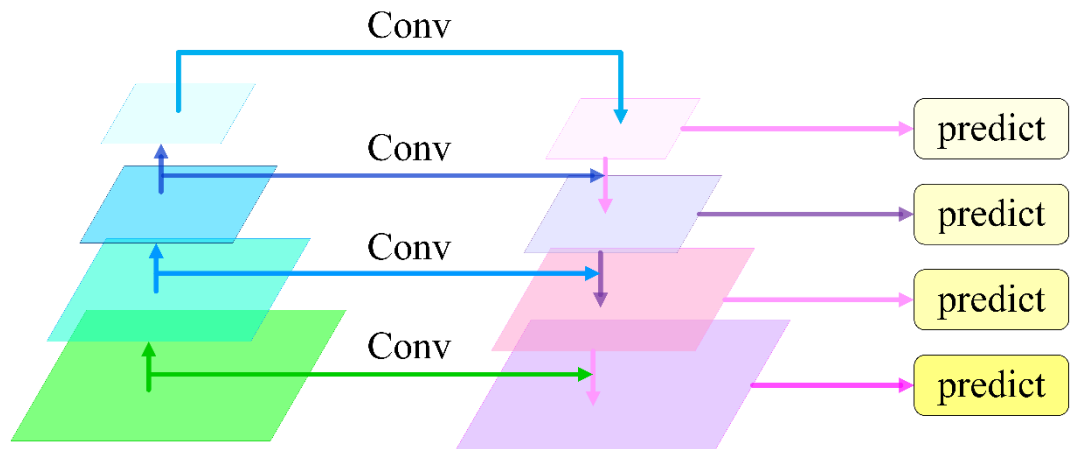


Figure 1. The structure of the raw feature pyramid network for object detection.

Therefore, in this paper, we introduce the feature pyramid network (FPN) [26] to tackle the above instinct limitation of encoder-decoder structures. As a top-down multi-scale feature fusion scheme, the feature pyramid [26] aims at optimally combining low-level detailed spatial information and high-level abundant semantic features. Specifically,

with marginal extra consumption, FPN utilizes a pyramidal hierarchy to structure feature pyramids which comprise a bottom-up pathway and a top-down pathway. The bottom-up pathway usually adopts the ResNet [27] pre-trained on ImageNet as the backbone, while the top-down pathway is normally equipped with lateral connections to construct high-level semantic features at multi-scales. As a generic feature extractor, the FPN architecture has shown significant improvement [26]. However, the raw FPN is initially designed for object detection which cannot directly be utilized to semantic segmentation. Meanwhile, the context information is not considered of the FPN which is crucial for segmentation. Hence, based on our previous research on the linear attention mechanism [28], we develop a multi-head attention module (MHA) to thoroughly capture the global context information and greatly merge the multi-scale feature maps. The main contributions of this paper are listed as follows:

- We introduce the feature pyramid network (FPN) which substitutes the conventional encoder-decoder structure and effectively combines the extracted spatial and contextual features to improve the performance of semantic segmentation.
- For transforming the FPN from detection structure to segmentation structure, we design a multi-head attention module (MHA) which not only extracts the global context information but also fuses the multi-scale feature maps.
- Based on the FPN and MHA, we develop a feature pyramid network with multi-head attention (FPN-MHA) for semantic segmentation of fine-resolution remotely sensed images. The comprehensive experiments demonstrate the effectiveness of our FPN-MHA.

2. Related Work

2.1. Feature Pyramid Network

The feature pyramid network (FPN) is initially designed for object detection, aiming at leveraging the pyramidal feature hierarchy [26]. Specifically, the FPN contains semantics from low-level to high-level, constructing the feature pyramid with high-level semantics throughout. The components of the FPN comprise a bottom-up pathway, a top-down pathway, and lateral connections, as shown in Figure 1. Concretely, the bottom-up pathway usually takes the ResNet [27] as the backbone, computing the feature hierarchy and generating feature maps at multi scales. The feature maps contained in higher pyramid levels are spatially coarser but semantically stronger. The top-down pathway hallucinates finer resolution features by upsampling higher feature maps, which are then merged and refined with features from the paratactic bottom-up pathway via lateral connections. Particularly, the feature maps from the bottom-up and top-down pathways fused by the lateral connection are in the same spatial size. The effectiveness of FPN has been verified in several applications including object detection [26], panoptic segmentation [29], and super-resolution [30].

2.2. Semantic Segmentation

The goal of semantic segmentation from fine-resolution remotely sensed images is to assign each pixel of imagery an accurate ground object class, which is a pillar of several applications such as infrastructure management, urban planning, and economic assessment [18,31,32]. Recently, deep learning methods have shown their tremendous potential for segmentation. After the first successful Fully Convolutional Network (FCN), DilatedFCN and EncoderDecoder are two subsequently promising directions. The DilatedFCNs [16-18] harness dilate or atrous convolutions to retain the receptive fields and utilize the multi-scale context module to process high-level features. Alternatively, EncoderDecoders [10,14,15] employ the encoder to extract multi-level features and fused them with the upsampled features for final prediction via the decoder. Significantly, more and more endeavors [21,28] are made to combine the merits between the DilatedFCNs and EncoderDecoders.

In recent years, with the advance of technology, semantic segmentation plays more and more important roles in many practical scenarios, especially for remote sensing applications, such as road detection [33,34], urban resources management [35,36], and land-

use mapping [37,38]. A novel CNN-based multistage framework is introduced by [33] to extract road surface and centerline tracing simultaneously. By continuously increasing the patch scale, Zhang et al. [35] characterizes and classifies individual plants based on segmentation methods. For land-use mapping, the recently developed semantic segmentation algorithms using deep learning create a new paradigm [37,38].

2.3. The Attention Mechanism

The accuracy of segmentation highly hinges on sufficient context information. To this end, the dot-product attention mechanism is introduced to capture global context information. However, the high memory and computational consumptions which increase quadratically with the input size heavily hinder the application prospect of the dot-product attention mechanism. In this part, we illustrate the principles of the dot-product attention mechanism as well as the attempts to reduce the complexity of the attention mechanism. By default, vectors in this section are column vectors.

2.3.1 The Dot-Product Attention Mechanism

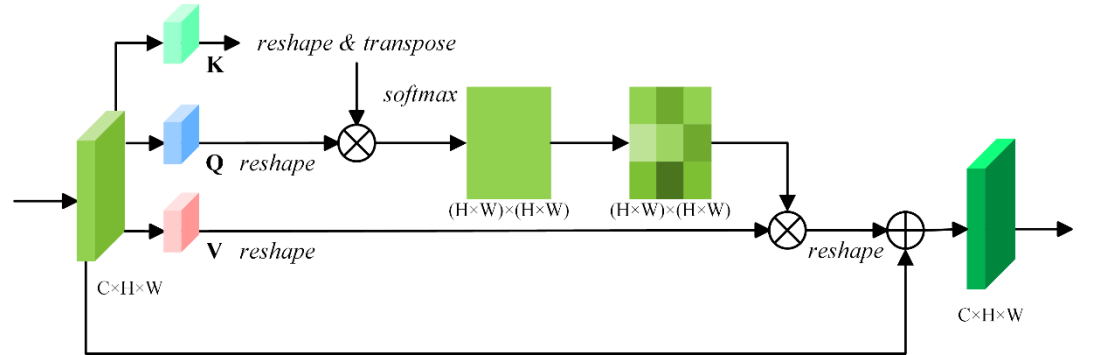


Figure 2. The diagram of the dot-product attention modified for computer vision.

Supposing the height, weight, and channels of the input are denoted as H , W , and C , respectively, while $\mathbf{X} = [\mathbf{x}_1, \dots, \mathbf{x}_N] \in \mathbb{R}^{N \times C}$ is the input feature, where $N = H \times W$. Firstly, the dot-product attention mechanism harnesses three projected matrices $\mathbf{W}_q \in \mathbb{R}^{D_x \times D_k}$, $\mathbf{W}_k \in \mathbb{R}^{D_x \times D_k}$, and $\mathbf{W}_v \in \mathbb{R}^{D_x \times D_v}$ to obtain the query matrix \mathbf{Q} , key matrix \mathbf{K} , and value matrix \mathbf{V} :

$$\begin{cases} \mathbf{Q} = \mathbf{XW}_q \in \mathbb{R}^{N \times D_k}; \\ \mathbf{K} = \mathbf{XW}_k \in \mathbb{R}^{N \times D_k}; \\ \mathbf{V} = \mathbf{XW}_v \in \mathbb{R}^{N \times D_v}. \end{cases} \quad (1)$$

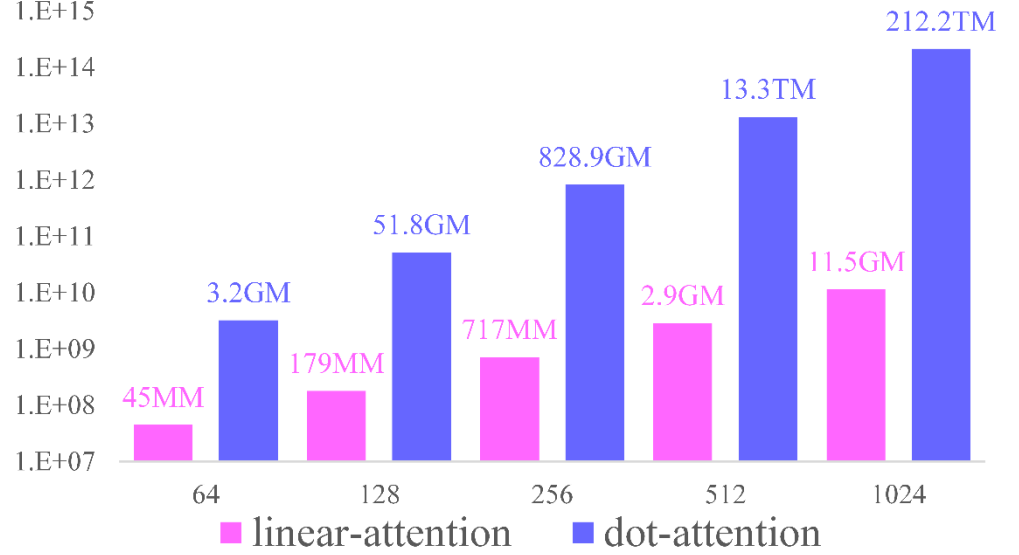
\mathbf{Q} and \mathbf{K} are supposed to be in identical shape. Subsequently, in order to calculate the similarity between the i -th query feature $\mathbf{q}_i^T \in \mathbb{R}^{D_k}$ and the j -th key feature $\mathbf{k}_j \in \mathbb{R}^{D_k}$, a normalization function ρ is employed as $\rho(\mathbf{q}_i^T \mathbf{k}_j) \in \mathbb{R}^1$. Thereafter, similarities between all pairs of pixels are computed and taken as weights. Accordingly, the output is generated by aggregating all positions using weighted summation:

$$\mathbf{D}(\mathbf{Q}, \mathbf{K}, \mathbf{V}) = \rho(\mathbf{QK}^T)\mathbf{V}. \quad (2)$$

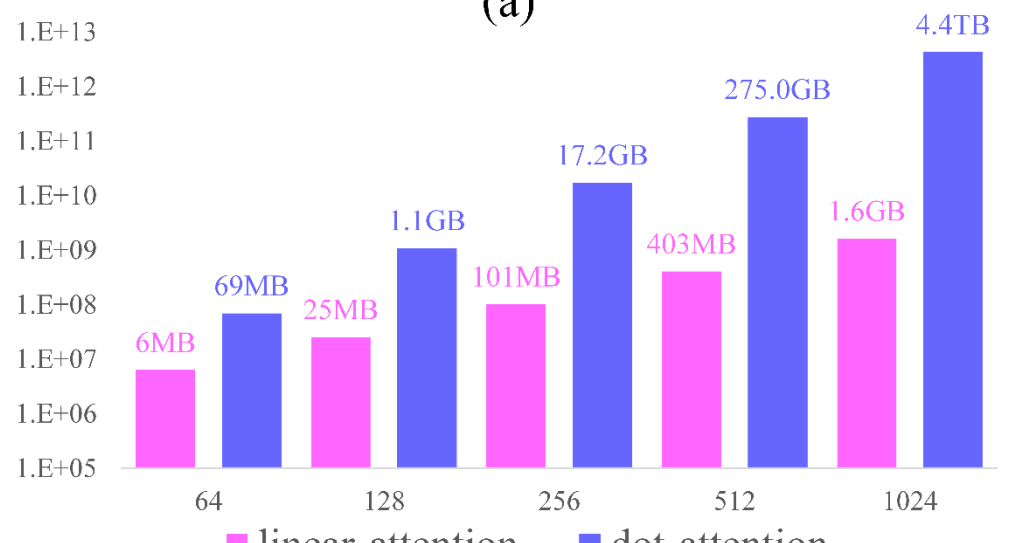
Normally, the normalization function is set as softmax:

$$\rho(\mathbf{Q}^T \mathbf{K}) = \text{softmax}_{\text{row}}(\mathbf{QK}^T), \quad (3)$$

where $\text{softmax}_{\text{row}}$ denotes that the softmax is operated along the row of matrix \mathbf{QK}^T .



(a)



(b)

Figure 3. The (a) computation requirement and (b) memory requirement between the linear attention mechanism and dot-product attention mechanism under different input sizes. The calculation assumes $C = D_v = 2D_k = 64$. Please notice that the figure is on the log scale.

By modeling the similarities among all pairs of pixels in the input, the global context information can be entirely captured by the $\rho(\mathbf{Q}\mathbf{K}^T)$. The dot-product attention mechanism is initially proposed for machine translation [39], whereafter be introduced and modified for computer vision by the non-local module (Figure 2) [40]. However, as $\mathbf{Q} \in \mathbb{R}^{N \times D_k}$ and $\mathbf{K}^T \in \mathbb{R}^{D_k \times N}$, the multiplication between \mathbf{Q} and \mathbf{K}^T belongs to $\mathbb{R}^{N \times N}$, leading to the $O(N^2)$ time and memory complexity. Based on the dot-product attention mechanism and its variants, many attention-based networks has been proposed successively to tackle the semantic segmentation task, such as Dual Attention Network (DANet) [22], Object Context Network (OCNet) [41], and Co-occurrence Feature Network (CFNet) [42].

2.3.2 Generalization and Simplification

Supposing the normalization function is softmax, the i -th row in the output matrix produced by the dot-product attention mechanism can be written as:

$$D(\mathbf{Q}, \mathbf{K}, \mathbf{V})_i = \frac{\sum_{j=1}^N e^{\mathbf{q}_i^T \mathbf{k}_j} \mathbf{v}_j}{\sum_{j=1}^N e^{\mathbf{q}_i^T \mathbf{k}_j}}. \quad (4)$$

Equation (4) can be generalized to any normalization function as:

$$D(\mathbf{Q}, \mathbf{K}, \mathbf{V})_i = \frac{\sum_{j=1}^N \text{sim}(\mathbf{q}_i, \mathbf{k}_j) \mathbf{v}_j}{\sum_{j=1}^N \text{sim}(\mathbf{q}_i, \mathbf{k}_j)}, \quad (5)$$

$$\text{sim}(\mathbf{q}_i, \mathbf{k}_j) \geq 0.$$

$\text{sim}(\mathbf{q}_i, \mathbf{k}_j)$ depicts the similarity between the \mathbf{q}_i and \mathbf{k}_j , which can be expanded as $\phi(\mathbf{q}_i)^T \varphi(\mathbf{k}_j)$. Whereupon, we can rewrite equation (4) to equation (6) and then simplify as equation (7):

$$D(\mathbf{Q}, \mathbf{K}, \mathbf{V})_i = \frac{\sum_{j=1}^N \phi(\mathbf{q}_i)^T \varphi(\mathbf{k}_j) \mathbf{v}_j}{\sum_{j=1}^N \phi(\mathbf{q}_i)^T \varphi(\mathbf{k}_j)}, \quad (6)$$

$$D(\mathbf{Q}, \mathbf{K}, \mathbf{V})_i = \frac{\phi(\mathbf{q}_i)^T \sum_{j=1}^N \varphi(\mathbf{k}_j) \mathbf{v}_j^T}{\phi(\mathbf{q}_i)^T \sum_{j=1}^N \varphi(\mathbf{k}_j)}. \quad (7)$$

In particular, equation (5) is identical to equation (4) when $\phi(\cdot) = \varphi(\cdot) = e^{(\cdot)}$. The equation (7) can be represented as the vectorized form:

$$D(\mathbf{Q}, \mathbf{K}, \mathbf{V}) = \frac{\phi(\mathbf{Q}) \varphi(\mathbf{K})^T \mathbf{V}}{\phi(\mathbf{Q}) \sum_j \varphi(\mathbf{K})_{i,j}^T}. \quad (8)$$

As $\text{sim}(\mathbf{q}_i, \mathbf{k}_j) = \phi(\mathbf{q}_i)^T \varphi(\mathbf{k}_j)$ replaces the softmax function, we can then alter the order of the commutative operation, thereby shunning the computationally intensive operation. To be specific, the multiplication between $\varphi(\mathbf{K})^T$ and \mathbf{V} can be computed first and then multiply the result and \mathbf{Q} , resulting in only $O(dN)$ time and memory complexity. The appropriate $\phi(\cdot)$ and $\varphi(\cdot)$ enable the above solution to dramatically reduce resource consumption without lowering the accuracy [15,25].

2.3.3 The Linear Attention Mechanism

By substituting the softmax to its first-order approximation of Taylor expansion, we developed a linear attention mechanism in our previous research [28] as:

$$e^{\mathbf{q}_i^T \mathbf{k}_j} \approx 1 + \mathbf{q}_i^T \mathbf{k}_j. \quad (9)$$

However, the above approximation cannot guarantee the nonnegative property of the normalization function. Hence, we normalize \mathbf{q}_i and \mathbf{k}_j by l_2 norm to ensure $\mathbf{q}_i^T \mathbf{k}_j \geq -1$:

$$\text{sim}(\mathbf{q}_i, \mathbf{k}_j) = 1 + \left(\frac{\mathbf{q}_i}{\|\mathbf{q}_i\|_2} \right)^T \left(\frac{\mathbf{k}_j}{\|\mathbf{k}_j\|_2} \right). \quad (10)$$

Then, we can rewrite equation (5) to equation (11) and simplify it to equation (12):

$$D(\mathbf{Q}, \mathbf{K}, \mathbf{V})_i = \frac{\sum_{j=1}^N \left(\mathbf{1} + \left(\frac{\mathbf{q}_i}{\|\mathbf{q}_i\|_2} \right)^T \left(\frac{\mathbf{k}_j}{\|\mathbf{k}_j\|_2} \right) \right) \mathbf{v}_j}{\sum_{j=1}^N \left(\mathbf{1} + \left(\frac{\mathbf{q}_i}{\|\mathbf{q}_i\|_2} \right)^T \left(\frac{\mathbf{k}_j}{\|\mathbf{k}_j\|_2} \right) \right)}, \quad (11)$$

$$D(\mathbf{Q}, \mathbf{K}, \mathbf{V})_i = \frac{\sum_{j=1}^N \mathbf{v}_j + \left(\frac{\mathbf{q}_i}{\|\mathbf{q}_i\|_2} \right)^T \sum_{j=1}^N \left(\frac{\mathbf{k}_j}{\|\mathbf{k}_j\|_2} \right) \mathbf{v}_j^T}{N + \left(\frac{\mathbf{q}_i}{\|\mathbf{q}_i\|_2} \right)^T \sum_{j=1}^N \left(\frac{\mathbf{k}_j}{\|\mathbf{k}_j\|_2} \right)}. \quad (12)$$

The vectorized form of equation (12) is:

$$D(\mathbf{Q}, \mathbf{K}, \mathbf{V}) = \frac{\sum_j \mathbf{V}_{i,j} + \left(\frac{\mathbf{Q}}{\|\mathbf{Q}\|_2} \right) \left(\left(\frac{\mathbf{K}}{\|\mathbf{K}\|_2} \right)^T \mathbf{V} \right)}{N + \left(\frac{\mathbf{Q}}{\|\mathbf{Q}\|_2} \right) \sum_j \left(\left(\frac{\mathbf{K}}{\|\mathbf{K}\|_2} \right)^T \right)_{i,j}}. \quad (13)$$

As $\sum_{j=1}^N \left(\frac{\mathbf{k}_j}{\|\mathbf{k}_j\|_2} \right) \mathbf{v}_j^T$ and $\sum_{j=1}^N \left(\frac{\mathbf{k}_j}{\|\mathbf{k}_j\|_2} \right)$ could be computed only once and then reused for each query, time and space complexity of the linear attention mechanism based on equation (13) is $O(dN)$. Please refers to [28] for more information about the linear attention mechanism.

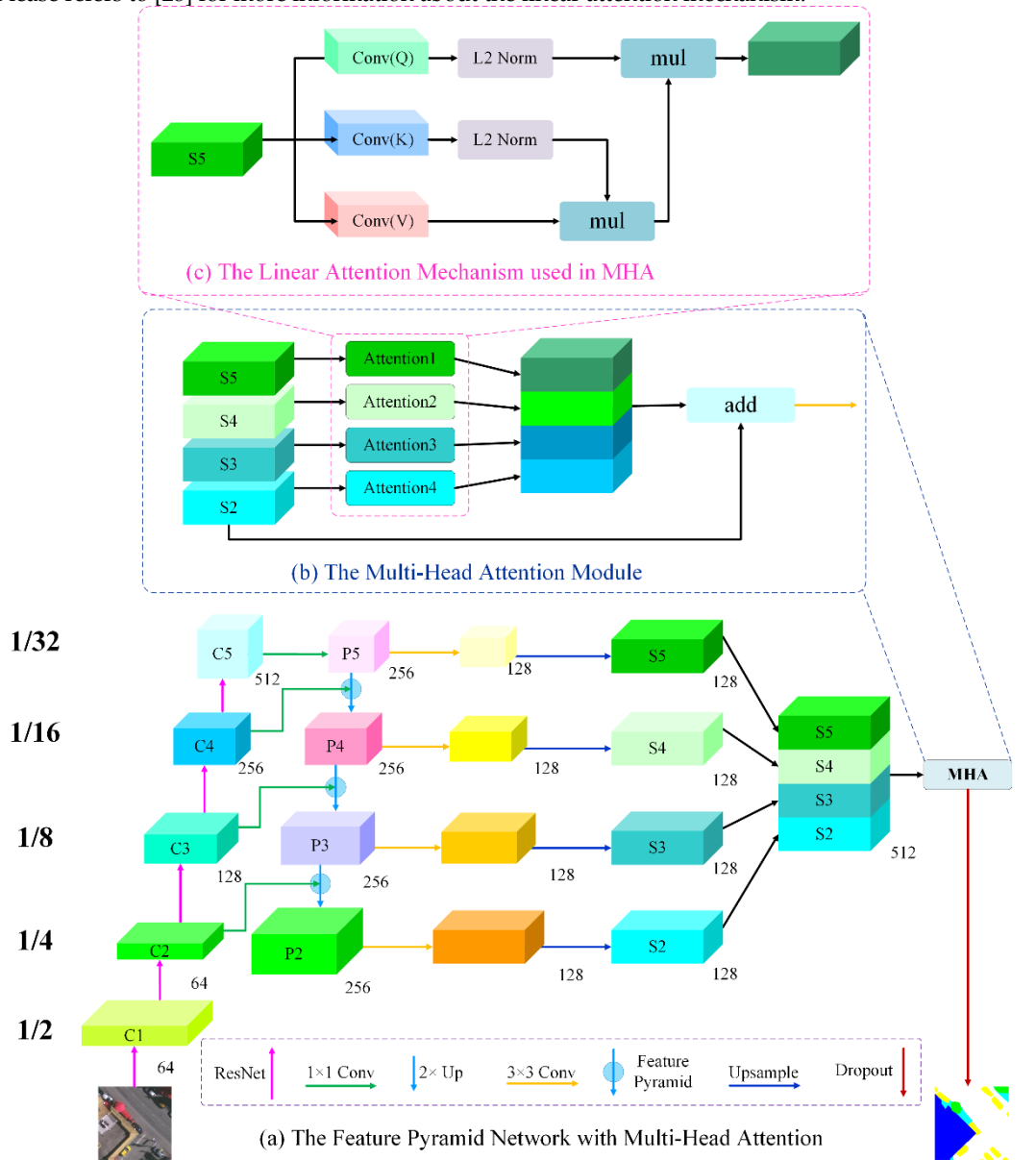


Figure 4. The structure of (a) the overall framework of our FPN-MHA, (b) the multi-head attention module, and (c) the linear attention mechanism (taking the attention1 as an example). The figures (e.g., 64, 128, 512) near the features indicate the number of channels.

3. Feature Pyramid Network with Multi-Head Attention

3.1. The Overall Framework

The overall framework of the proposed feature pyramid network with multi-head attention (FPN-MHA) is demonstrated in Figure 4. As a single end-to-end network, the main components of our FPN-MHA include the bottom-up pathway (i.e., the first column in Figure 4a), the feature pyramid (i.e., the second and third columns in Figure 4a), and the multi-head attention module (i.e., Figure 4b). We will elaborate on each component below.

3.2. The Bottom-Up Pathway

To design a simple and efficient framework, we select the ResNet34 as the backbone of the bottom-up pathway rather than the complicated backbones such as ResNet101. Based on the ResNet34, the bottom-up pathway performs the feedforward computation and generates the feature hierarchy. The generated feature maps are at different spatial resolutions with a scaling step of 2. The top levels of feature maps have more context information with lower resolution while the bottom levels of feature maps have less context information with higher resolution. We use C2, C3, C4, and C5 to indicate the output feature map of each residual block in ResNets (see above Figure 4), while the spatial size of C2, C3, C4, and C5 are 1/4, 1/8, 1/16, and 1/32 of the input size, respectively. Due to its large memory footprint, the C1 is not included in the pyramid.

3.3. The Top-Down Pathway and Lateral Connections

The top-down pathway upsamples semantically richer but spatially coarser feature maps from higher pyramid levels to hallucinate higher resolution features, which are then merged and refined with corresponding features from the bottom-up pathway by lateral connections. As can be seen from Figure 5, a top-down layer and a lateral connection constitute a feature pyramid in the proposed FPN-MHA. Accordingly, the generated feature maps are denoted as P2, P3, P4, and P5. Taking Figure 5 as an example, with a coarser-resolution feature map (e.g., P4 in Figure 5), we firstly upsample its spatial resolution by a factor of 2 (the upsampling mode is set as the nearest neighbor for simplicity). By element-wise addition, the upsampled map is then fused with the corresponding map (with a 1×1 convolutional layer to reduce dimensions of the channel) in the bottom-up pathway.

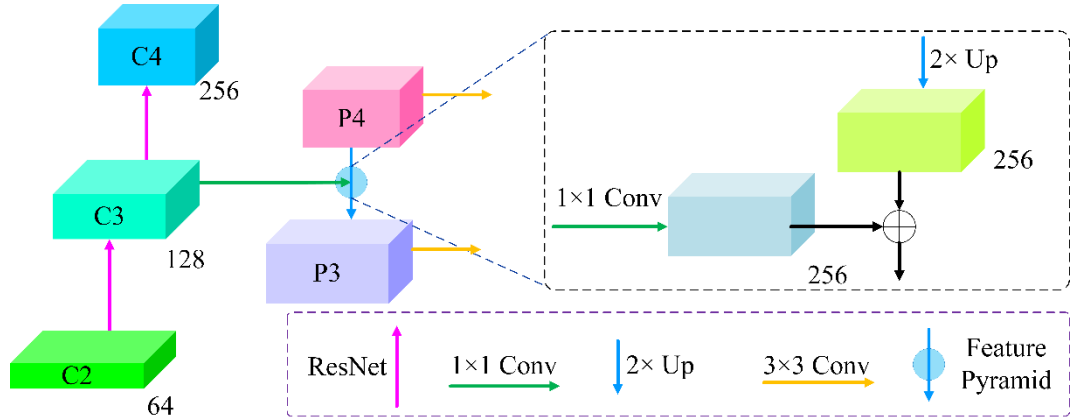


Figure 5. The feature pyramid in the proposed FPN-MHA.

The above procedure is iterated until generating the finest resolution map. To start the iteration, the coarsest resolution map (e.g., P5 in Figure 4) is simply produced by a 1×1 convolutional layer on C5. After the merged map has been generated by the corresponding feature pyramid, a 3×3 convolution is attached to produce the final feature map, aiming at mitigating the aliasing effect caused by upsampling. The feature pyramid combines low-level contextual information into low-level spatial feature maps, which improves the representation capability of low-level side networks. Concretely, interpreting different

scales of land covers requires different levels of context information. Obviously, there is more context information contained in the high-level features than the low-level features as the deeper convolution layers have larger receptive fields than these shallower ones. Hence, when merged with high-level features, the low-level side networks acquire the multi-scale context information to improve its accuracy of segmentation.

3.4. The Multi-Head Attention Module

As the FPN is initially proposed for object detection which cannot be directly utilized for semantic segmentation, we design the multi-head attention module (MHA) based on the linear attention mechanism as shown in Figure 4b and Figure 4c to enhance the global context information for segmentation. With four feature maps (i.e., S2, S3, S4, and S5) generated by the corresponding feature pyramid, the MHA contains four attention heads to extract long-range dependencies from each feature map. Whereafter, the generated feature maps are added to the origin input, which can be formulated as:

$$\text{head}_i = \text{Linear Attention}(\mathbf{X}_i \mathbf{W}_{q,i}, \mathbf{X}_i \mathbf{W}_{k,i}, \mathbf{X}_i \mathbf{W}_{v,i}), \quad (14)$$

$$\text{MHA} = \text{Concat}_i(\text{head}_i) \mathbf{W}_o, \quad (15)$$

where \mathbf{W}_i and \mathbf{W}_o are parameter matrices.

3.5. The Loss Function

We select the mixed loss function to train our FPN-MHA. To be specific, we fuse the cross-entropy loss and the focal loss via a simple weighted scheme:

$$\text{loss}_{CE}(p, y) = -y \log(p) - (1 - y) \log(1 - p), \quad (16)$$

$$\text{loss}_{focal}(p, y) = -y(1 - p)^\gamma \log p - (1 - y)p^\gamma \log(1 - p), \quad (17)$$

$$\text{loss}(p, y) = \alpha \text{loss}_{CE} + \beta \text{loss}_{focal}(p, y), \quad (18)$$

where y is the ground truth and p is the prediction generated by the network. γ which is set as 2 denotes the focusing parameter to controls the down-weighting of the easily classified examples. α and β indicate the weighting coefficients of the cross-entropy loss and the focal loss, which are set as 0.7 and 0.3 in our experiments, respectively. Please notice that for a fair comparison, the mixed loss function is adopted for all comparative methods.

4. Experimental Results

4.1. Datasets

We verify the effectiveness of our FPN-MHA based on the ISPRS Potsdam dataset and the ISPRS Vaihingen dataset (<http://www2.isprs.org/commissions/comm3/wg4/se-mantic-labeling.html>).

Vaihingen: There are 33 tiles that are extracted from true orthophotos and the corresponding registered normalized digital surface models (DSMs) in the Vaihingen dataset. The ground sampling distance (GSD) of tiles in Vaihingen is 9 cm and the average size is 2494 × 2064 pixels. We utilize tiles: 2, 4, 6, 8, 10, 12, 14, 16, 20, 22, 24, 27, 29, 31, 33, 35, 38 for testing, tile: 30 for validation, and the remaining 15 images for training. Please note that we only use the near-infrared, red, and green channels without DSM in our experiments.

Potsdam: The Potsdam contains There are 38 tiles extracted from true orthophotos and the corresponding registered normalized DSMs. The GSD of tiles in Potsdam is 5 cm and the size of each tile is 6000 × 6000. We utilize tiles: 2_13, 2_14, 3_13, 3_14, 4_13, 4_14, 4_15, 5_13, 5_14, 5_15, 6_13, 6_14, 6_15, 7_13 for testing, tile: 2_10 for validation, and the remaining 22 tiles, except 7_10 with error annotations, for training. The DSM is not employed in our experiments.

4.2. Evaluation Metrics

The performance of our FPN-MHA, as well as comparative methods, is measured by the overall accuracy (OA), the mean Intersection over Union (mIoU), and the F1 score (F1). Based on the accumulated confusion matrix, the OA, mIoU, and F1 are computed as:

$$OA = \frac{\sum_{k=1}^N TP_k}{\sum_{k=1}^N TP_k + FP_k + TN_k + FN_k}, \quad (19)$$

$$mIoU = \frac{1}{N} \sum_{k=1}^N \frac{TP_k}{TP_k + FP_k + FN_k}, \quad (20)$$

$$F1 = 2 \times \frac{precision \times recall}{precision + recall}, \quad (21)$$

where TP_k , FP_k , TN_k , and FN_k indicate the true positive, false positive, true negative, and false negatives, respectively, for object indexed as class k . OA is computed for all categories including the background.

4.3. Experimental Setting

We implemented the proposed FPN-MHA as well as comparative algorithms with PyTorch and trained them using a single Tesla V100 with 32 batch size and AdamW optimizer. The learning rate is set as 0.0003. For training, we cropped the original tiles into 512 \times 512 patches and augmented them by rotating, resizing, horizontal axis flipping, vertical axis flipping, and adding random noise. For comparisons, we considered not only the methods proposed initially for natural images, such as pyramid scene parsing network (PSPNet) [19] and dual attention network (DANet) [22], but also the models designed for remote sensing images, like edge-aware neural network (EaNet) [16]. Besides, U-Net [10], DABNet [43], BiSeNetV2 [44], and CE-Net [45] are also taken into comparison. The test time augmentation (TTA) in terms of rotating and flipping is applied for all algorithms.

4.4. Ablation Study

We conducted ablation experiments to verify the effectiveness of FPN and MHA in the proposed FPN-MHA. The encoder-decoder structure based on ResNet34 is selected as the baseline. As can be seen from Table 1, the performance of the Feature Pyramid Network (FPN) significantly overmatches the encoder-decoder baseline. For the Vaihingen dataset, the introduction of FPN brings more than 3.8% in mean F1 score, 1.2% in OA, and 3.6% in mIoU, while the improvements for the Potsdam dataset is 0.5%, 0.7%, and 0.7%, respectively. However, the FPN is initially designed for object detection. To tackle the segmentation issue, the feature maps generated by feature pyramids are simply summed, lacking the global context information which is crucial for segmentation. Therefore, the multi-head attention module (MHA) is developed to remedy the above limitation. As a specifically designed module for semantic segmentation, the utilization of MHA contributes to the increase of more than 0.5% in mean F1 score, 0.4% in OA, and 1.0% in mIoU for the Vaihingen dataset, while the figures for the Potsdam dataset are more than 0.8%, 0.7%, and 1.5%, respectively.

Table 1. The ablation study about FPN and MHA.

Dataset	Method	Backbone	Mean F1	OA (%)	mIoU
Vaihingen	Baseline	ResNet34	85.897	89.495	78.520
	FPN	ResNet34	89.716	90.712	82.184
	FPN-MHA	ResNet34	90.290	91.114	83.276
Potsdam	Baseline	ResNet34	91.138	89.471	86.734
	FPN	ResNet34	91.683	90.209	87.441
	FPN-MHA	ResNet34	92.555	90.949	88.998

4.5. Results on the ISPRS Vaihingen Dataset

We compare our method with seven existing methods on the Vaihingen test set and quantitative comparisons are shown in Table 2. Notably, for a fair comparison, the backbone of ResNet-based algorithms is uniformly set as ResNet34. It can be seen that our FPN-MHA outperforms other encoder-decoder methods (e.g., U-Net and CE-Net), attention-based methods (e.g., DANet), and context aggregation methods (e.g., PSPNet and EaNet) by a significant margin. To be specific, there are at least 1.8% in mean F1 score, 0.7% in OA, and 1.7% in mIoU which are higher than the other comparative methods. Especially, the F1 score of Car predicted by our FPN-MHA is much better than other approaches, which improves the second-best CE-Net by 6.4%, which demonstrates the effectiveness of the multi-head attention module. Meanwhile, we report the Kappa z-test which can evaluate the statistical significance between different methods which can be calculated by:

$$z = (k_1 - k_2) / \sqrt{v_1 + v_2} \quad (22)$$

where k indicates the Kappa coefficient and v represents the Kappa variance. The two comparative algorithms are signally different at the 95 % confidence level when the value of z is greater than 1.96. As experimental results are shown in Table 3, the scores demonstrate that our FPN-MHA delivers a robust performance which significantly outperforms other networks.

Table 2. The experimental results on the Vaihingen dataset.

Method	Backbone	Imp. surf.	Building	Low veg.	Tree	Car	Mean F1	OA (%)	mIoU (%)
U-Net	-	84.331	86.479	73.132	83.886	40.825	73.731	82.023	61.362
DABNet	-	87.775	88.808	74.319	84.905	60.247	79.211	84.278	67.373
BiSeNetV2	-	89.884	91.911	82.020	88.271	71.417	84.701	87.972	75.005
PSPNet	ResNet34	90.273	94.218	82.757	88.606	51.100	81.391	88.82	71.591
DANet	ResNet34	91.135	94.818	83.467	88.923	62.979	84.264	89.524	74.728
EaNet	ResNet34	92.172	95.197	82.811	89.254	80.563	87.999	89.995	80.223
CE-Net	ResNet34	92.681	95.529	83.359	89.492	81.243	88.461	90.402	81.492
FPN-MHA	ResNet34	93.212	95.682	84.958	89.929	87.667	90.290	91.114	83.276

Table 3. The Kappa-z test on the Vaihingen dataset.

Method	K	KV ¹	DABNet	BiSeNetV2	PSPNet	DANet	EaNet	CE-Net	FPN-MHA
U-Net	0.77	3.14	12.33	39.15	39.59	43.83	47.52	50.40	54.34
DABNet	0.80	2.81	-	26.86	27.30	31.56	35.27	38.17	42.14
BiSeNetV2	0.86	2.08	-	-	0.45	4.73	8.47	11.40	15.42
PSPNet	0.86	2.07	-	-	-	4.28	8.02	10.95	14.97
DANet	0.87	1.96	-	-	-	-	3.74	6.67	10.69
EaNet	0.87	1.86	-	-	-	-	-	2.93	6.96
CE-Net	0.88	1.79	-	-	-	-	-	-	4.03
FPN-MHA	0.89	1.68	-	-	-	-	-	-	-

¹ The unit of the Kappa variance (KV) is 10^{-9} .

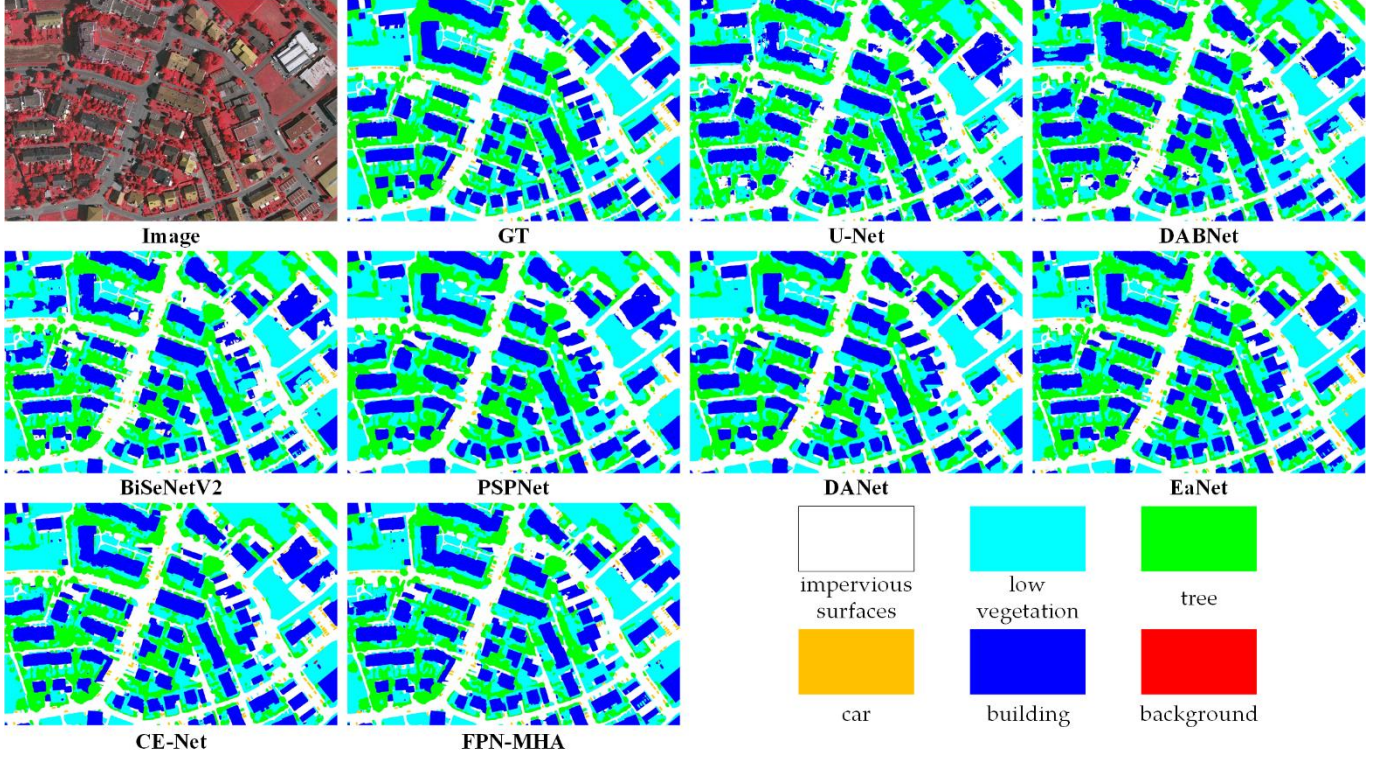


Figure 6. Visualization of tile-38 in the Vaihingen dataset.

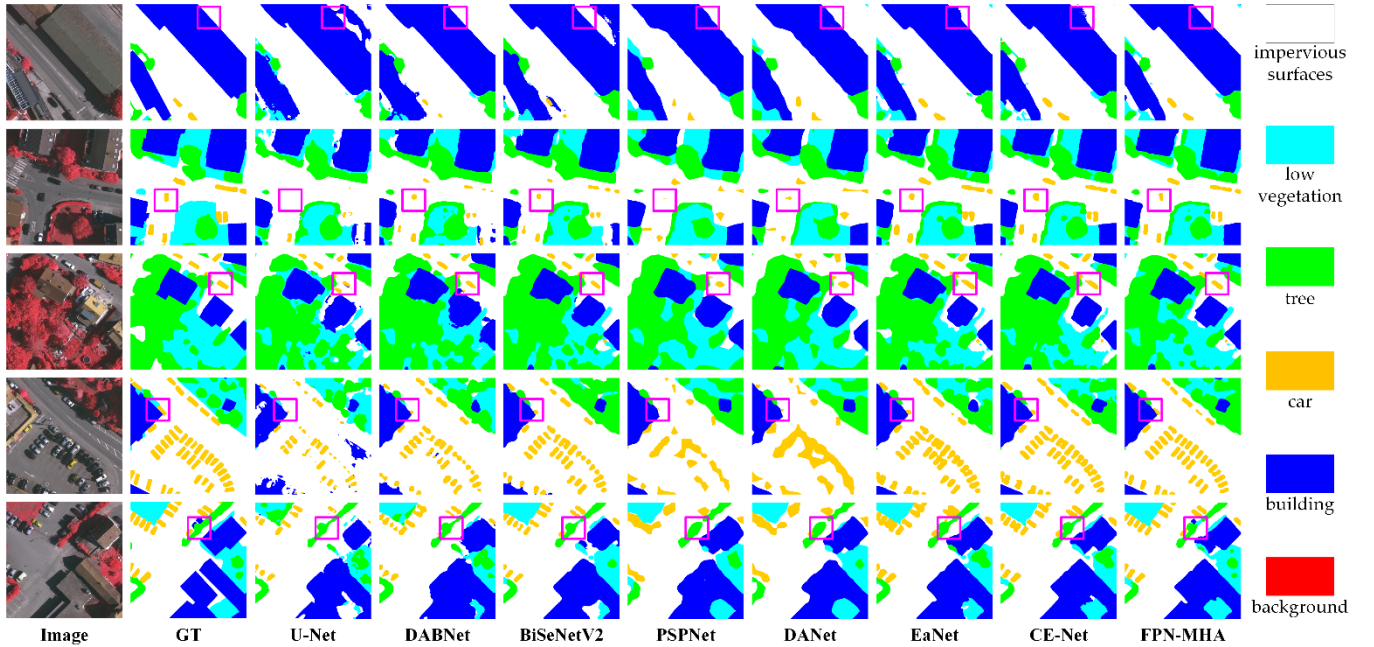


Figure 7. Visualization of results on the Vaihingen dataset.

4.6. Results on the ISPRS Potsdam Dataset

To further evaluate the effectiveness of FPN-MHA, we carry out experiments on the ISPRS Potsdam dataset. Empirically, the identical training and testing settings on the Potsdam dataset are identical to those on the Vaihingen dataset. Numerical comparisons with comparative algorithms are demonstrated in Table 4. Remarkably, FPN-MHA achieves 92.555% in mean F1 score, 90.949% in overall accuracy, and 87.28% in mIoU. Besides, the results of the Kappa-z test in Table 5 illustrate that our FPN-MHA is significantly superior to others. Further, in Figure 8, we visualize tile 3_13 in the Potsdam dataset in order to qualitatively verify the effectiveness of the proposed FPN-MHA, while the enlarged

512×512 patches can be seen in Figure 9. We mark the intractable regions with red boxes. It can be seen that FPN-MHA produces better segmentation results than other methods.

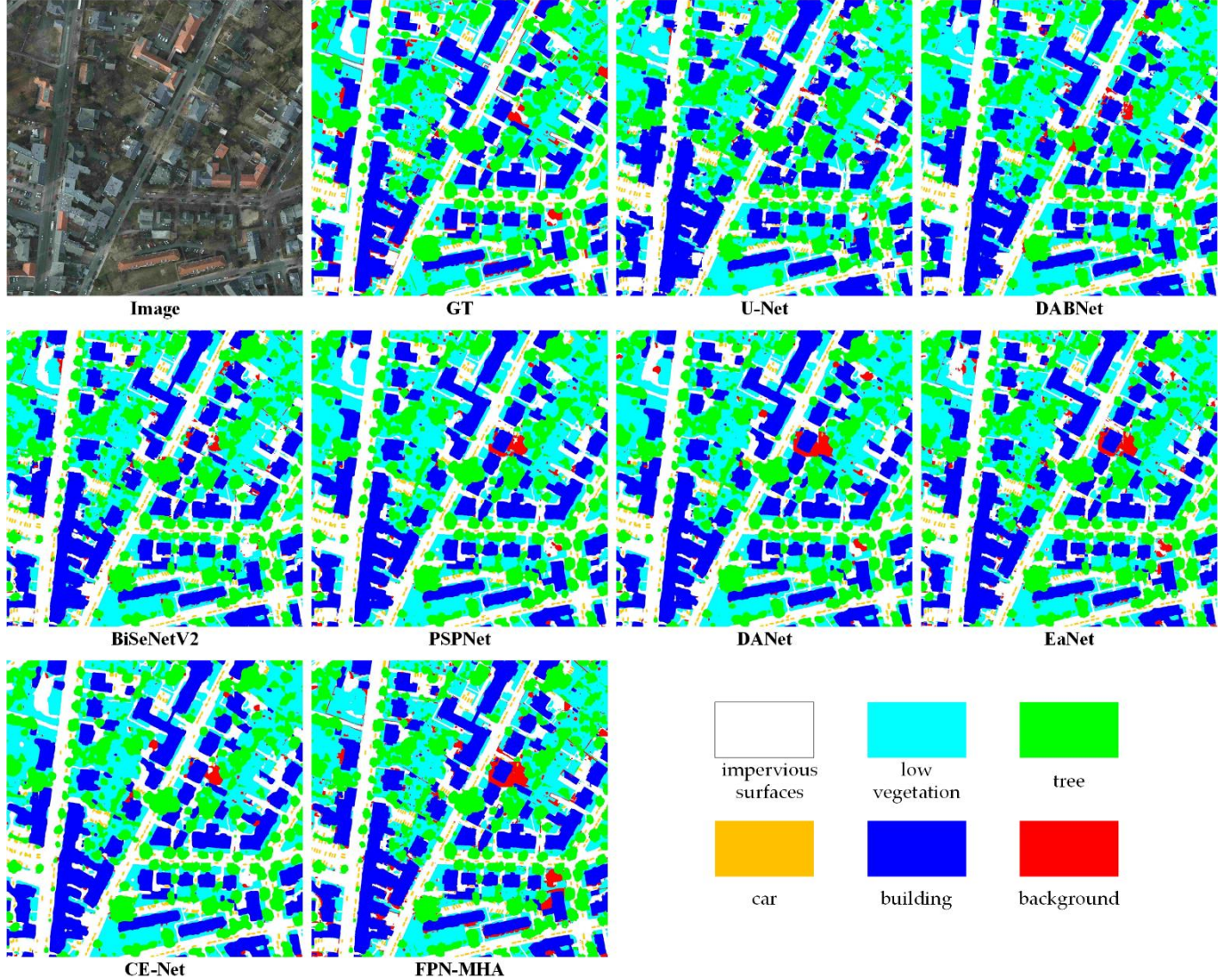


Figure 8. Visualization of tile-3_13 in the Potsdam dataset.

Table 4. The experimental results on the Potsdam dataset.

Method	Backbone	Imp. surf.	Building	Low veg.	Tree	Car	Mean F1	OA (%)	mIoU (%)
U-Net	-	84.992	88.822	76.741	73.116	90.328	82.800	80.614	74.300
DABNet	-	89.939	93.188	83.596	82.257	92.578	88.312	86.664	82.144
BiSeNetV2	-	91.280	94.316	85.048	85.192	94.112	89.990	88.174	85.167
DANet	ResNet34	91.624	95.835	85.955	87.704	86.471	89.518	89.469	83.574
PSPNet	ResNet34	91.911	96.121	85.625	87.643	86.844	89.629	89.562	83.754
EaNet	ResNet34	92.417	96.260	85.617	87.919	95.099	91.462	89.740	87.468
CE-Net	ResNet34	92.533	96.382	86.441	87.756	95.310	91.684	90.006	87.731
FPN-MHA	ResNet34	93.326	96.810	87.634	88.808	96.199	92.555	90.949	88.998

Table 5. The Kappa-z test on the Potsdam dataset.

Method	K	KV ¹	DABNet	BiSeNetV2	PSPNet	DANet	EaNet	CE-Net	FPN-MHA
U-Net	0.79	5.40	80.05	106.59	119.76	120.20	132.80	135.10	149.48
DABNet	0.86	3.71	-	26.89	40.26	40.60	53.71	56.04	70.84
BiSeNetV2	0.88	3.18	-	-	13.37	13.66	26.91	29.24	44.13

PSPNet	0.90	2.91	-	-	-	0.26	13.59	15.92	30.86
DANet	0.90	2.88	-	-	-	-	13.36	15.70	30.67
EaNet	0.91	2.68	-	-	-	-	-	2.32	17.24
CE-Net	0.91	2.63	-	-	-	-	-	-	14.93
FPN-MHA	0.92	2.35	-	-	-	-	-	-	-

¹The unit of the Kappa variance (KV) is 10^{-10} .

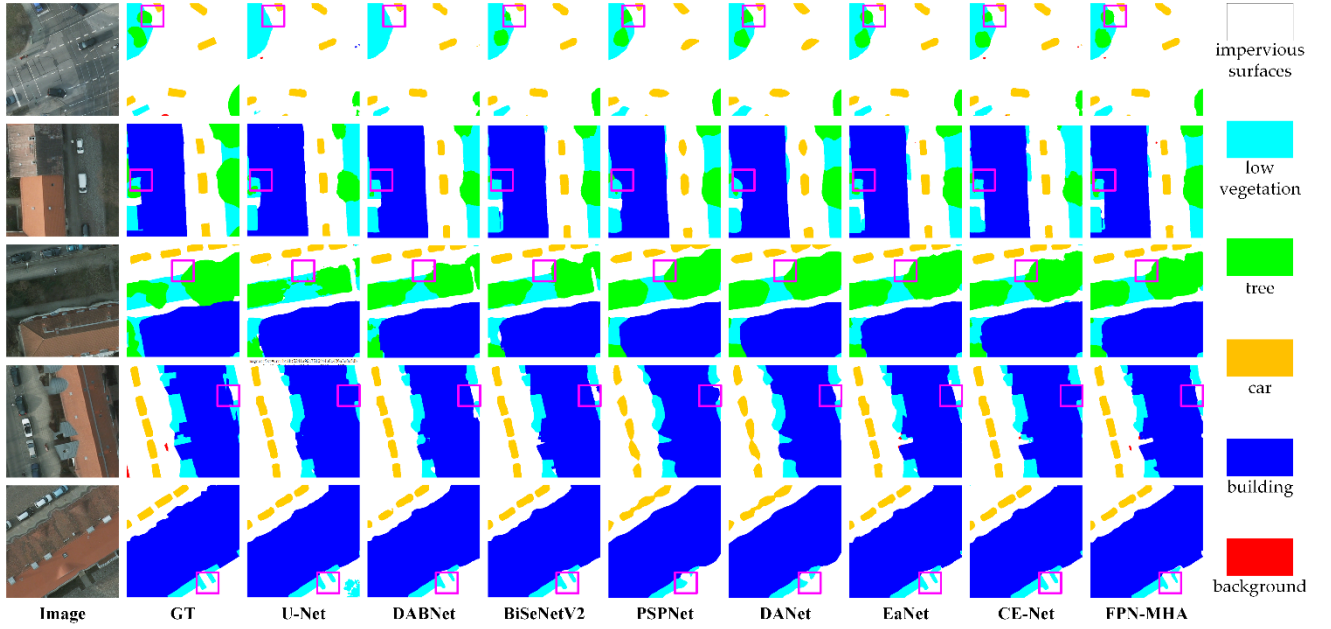


Figure 9. Visualization of results on the Potsdam dataset.

4.7. Limitation and Future Work

Even though the proposed FPN-MHA has bridged the left gap of feature fusion between the low-level and high-level features, there are still certain inherent pending issues that should be noticed. First, the total trainable parameters in the FPN-MHA are 28.72 M, which is less than medium-scale networks such as PSPNet (34.14 M), and EaNet (44.34 M) though larger than those small-scale networks like DANet (24.96 M) and BiSeNetV2 (12.30 M). Hence, the efficiency of our network is relatively slow, making the proposed FPN-MHA impractical to be utilized on mobile platforms. Second, it is obvious that more bands contain more information. Hence, as reported in [46], the specifically designed networks which fuse orthophoto (TOP) images with DSMs or NDSMs can easily achieve high performance. However, as the utilization of these auxiliary bands usually accompany with computationally intensive operation, we do not take DSM and NDSMs into consideration. Based on the above-mentioned limitations, our future work will hammer at achieving real-time semantic segmentation and fusing the DSMs or NDSMs to further enhance the segmentation performance.

5. Conclusion

Although enormous endeavors have been made, the automatic semantic segmentation from the fine-resolution remotely sensed images remains a complicated and challenging issue due to the limited spatial and contextual information. With such motivations, we introduce the Feature Pyramid Network (FPN) to completely combine the extracted spatial and contextual features and further develop the tremendous potential of the Convolutional Neural Network (CNN). Specifically, the pyramidal hierarchy enables FPN to thoroughly combining low-level detailed spatial information and high-level abundant semantic features. Besides, in order to transform the detection-oriented FPN to the segmentation-oriented structure, we propose a Multi-Head Attention module (MHA) which not only effectively merges the feature maps generated by the feature pyramid but also fully

extracts the global context information. Substantial experiments conducted on the ISPRS Potsdam and Vaihingen datasets demonstrate the effectiveness of our FPN-MHA and the extensive ablation studies illustrate the validity of FPN and MHA.

Author Contributions:

Funding: This research was funded by the National Natural Science Foundation of China (Nos. 41671452).

Institutional Review Board Statement: Not applicable.

Informed Consent Statement: Not applicable.

Data Availability Statement: No new data were created or analyzed in this study. Data sharing is not applicable to this article.

Acknowledgments: The authors thank ISPRS for providing the Potsdam and Vaihingen datasets.

Conflicts of Interest: The authors declare no conflicts of interest. The founding sponsors had no role in the design of the study; in the collection, analyses, or interpretation of data; in the writing of the manuscript; nor in the decision to publish the results.

Abbreviations

The following abbreviations are used in this manuscript:

CNN	Convolutional Neural Network
FCN	Fully-Convolutional Network
FPN	Feature Pyramid Network
MHA	Multi-Head Attention module
FPN-MHA	Feature Pyramid Network with Multi-Head Attention
CE	Cross-Entropy
ISPRS	International Society for Photogrammetry and Remote Sensing
OCNet	Object Context Network
CFNet	Co-occurrent Feature Network
PSPNet	Pyramid Scene Parsing Network
DANet	Dual Attention Network
CE-Net	Context Encoder Network
EaNet	Edge-aware Neural Network
BiSeNetV2	Bilateral Segmentation Network V2
DABNet	Depth-wise Asymmetric Bottleneck Network
OA	Overall Accuracy
mIoU	mean Intersection over Union
F1	F1 score
TTA	Test Time Augmentation
DSMs	Digital Surface Models
NDSMs	Normalized Digital Surface Models
GSD	Ground Sampling Distance
K	Kappa
KV	Kappa Variance

References

1. Li, R.; Duan, C. ABCNet: Attentive Bilateral Contextual Network for Efficient Semantic Segmentation of Fine-Resolution Remote Sensing Images. *arXiv preprint arXiv:2102.02531* **2021**.
2. Zhang, C.; Sargent, I.; Pan, X.; Li, H.; Gardiner, A.; Hare, J.; Atkinson, P.M. Joint Deep Learning for land cover and land use classification. *Remote sensing of environment* **2019**, *221*, 173-187.
3. Tong, X.-Y.; Xia, G.-S.; Lu, Q.; Shen, H.; Li, S.; You, S.; Zhang, L. Land-cover classification with high-resolution remote sensing images using transferable deep models. *Remote Sensing of Environment* **2020**, *237*, 111322.

4. Zhu, X.X.; Tuia, D.; Mou, L.; Xia, G.-S.; Zhang, L.; Xu, F.; Fraundorfer, F. Deep learning in remote sensing: A comprehensive review and list of resources. *IEEE Geoscience and Remote Sensing Magazine* **2017**, *5*, 8-36.
5. Duan, C.; Pan, J.; Li, R. Thick Cloud Removal of Remote Sensing Images Using Temporal Smoothness and Sparsity Regularized Tensor Optimization. *Remote Sensing* **2020**, *12*, 3446.
6. Zhang, C.; Harrison, P.A.; Pan, X.; Li, H.; Sargent, I.; Atkinson, P.M. Scale Sequence Joint Deep Learning (SS-JDL) for land use and land cover classification. *Remote Sensing of Environment* **2020**, *237*, 111593.
7. Li, R.; Zheng, S.; Duan, C.; Yang, Y.; Wang, X. Classification of Hyperspectral Image Based on Double-Branch Dual-Attention Mechanism Network. *Remote Sensing* **2020**, *12*, 582.
8. Gu, X.; Angelov, P.; Zhang, C.; Atkinson, P. A Semi-Supervised Deep Rule-Based Approach for Complex Satellite Sensor Image Analysis. *IEEE Transactions on Pattern Analysis and Machine Intelligence* **2020**.
9. Long, J.; Shelhamer, E.; Darrell, T. Fully convolutional networks for semantic segmentation. In Proceedings of Proceedings of the IEEE conference on computer vision and pattern recognition; pp. 3431-3440.
10. Ronneberger, O.; Fischer, P.; Brox, T. U-net: Convolutional networks for biomedical image segmentation. In Proceedings of International Conference on Medical image computing and computer-assisted intervention; pp. 234-241.
11. Badrinarayanan, V.; Kendall, A.; Cipolla, R. Segnet: A deep convolutional encoder-decoder architecture for image segmentation. *IEEE transactions on pattern analysis and machine intelligence* **2017**, *39*, 2481-2495.
12. Yu, F.; Koltun, V. Multi-scale context aggregation by dilated convolutions. *arXiv preprint arXiv:1511.07122* **2015**.
13. Chen, L.-C.; Papandreou, G.; Kokkinos, I.; Murphy, K.; Yuille, A.L. Semantic image segmentation with deep convolutional nets and fully connected crfs. *arXiv preprint arXiv:1412.7062* **2014**.
14. Rui, L.; Cehnxi, D.; Shunyi, Z. MACU-Net Semantic Segmentation from High-Resolution Remote Sensing Images. *arXiv preprint arXiv:2007.13083* **2020**.
15. Li, R.; Zheng, S.; Duan, C.; Su, J. Multi-Attention-Network for Semantic Segmentation of High-Resolution Remote Sensing Images. *arXiv preprint arXiv:2009.02130* **2020**.
16. Zheng, X.; Huan, L.; Xia, G.-S.; Gong, J. Parsing very high resolution urban scene images by learning deep ConvNets with edge-aware loss. *ISPRS Journal of Photogrammetry and Remote Sensing* **2020**, *170*, 15-28.
17. Wu, H.; Zhang, J.; Huang, K.; Liang, K.; Yu, Y. Fastfcn: Rethinking dilated convolution in the backbone for semantic segmentation. *arXiv preprint arXiv:1903.11816* **2019**.
18. Yang, H.; Yu, B.; Luo, J.; Chen, F. Semantic segmentation of high spatial resolution images with deep neural networks. *GIScience & Remote Sensing* **2019**, *56*, 749-768.
19. Zhao, H.; Shi, J.; Qi, X.; Wang, X.; Jia, J. Pyramid scene parsing network. In Proceedings of Proceedings of the IEEE conference on computer vision and pattern recognition; pp. 2881-2890.
20. Chen, L.-C.; Papandreou, G.; Schroff, F.; Adam, H. Rethinking atrous convolution for semantic image segmentation. *arXiv preprint arXiv:1706.05587* **2017**.
21. Chen, L.-C.; Zhu, Y.; Papandreou, G.; Schroff, F.; Adam, H. Encoder-decoder with atrous separable convolution for semantic image segmentation. In Proceedings of Proceedings of the European conference on computer vision (ECCV); pp. 801-818.
22. Fu, J.; Liu, J.; Tian, H.; Li, Y.; Bao, Y.; Fang, Z.; Lu, H. Dual attention network for scene segmentation. In Proceedings of Proceedings of the IEEE Conference on Computer Vision and Pattern Recognition; pp. 3146-3154.
23. Child, R.; Gray, S.; Radford, A.; Sutskever, I. Generating long sequences with sparse transformers. *arXiv preprint arXiv:1904.10509* **2019**.
24. Kitaev, N.; Kaiser, L.; Levskaya, A. Reformer: The efficient transformer. *arXiv preprint arXiv:2001.04451* **2020**.
25. Katharopoulos, A.; Vyas, A.; Pappas, N.; Fleuret, F. Transformers are RNNs: Fast Autoregressive Transformers with Linear Attention. *arXiv preprint arXiv:2006.16236* **2020**.
26. Lin, T.-Y.; Dollár, P.; Girshick, R.; He, K.; Hariharan, B.; Belongie, S. Feature pyramid networks for object detection. In Proceedings of Proceedings of the IEEE conference on computer vision and pattern recognition; pp. 2117-2125.

27. He, K.; Zhang, X.; Ren, S.; Sun, J. Deep residual learning for image recognition. In Proceedings of Proceedings of the IEEE conference on computer vision and pattern recognition; pp. 770-778.

28. Li, R.; Su, J.; Duan, C.; Zheng, S. Multistage Attention ResU-Net for Semantic Segmentation of Fine-Resolution Remote Sensing Images. *arXiv preprint arXiv:2011.14302* **2020**.

29. Kirillov, A.; Girshick, R.; He, K.; Dollár, P. Panoptic feature pyramid networks. In Proceedings of Proceedings of the IEEE/CVF Conference on Computer Vision and Pattern Recognition; pp. 6399-6408.

30. Shoeiby, M.; Armin, A.; Aliakbarian, S.; Anwar, S.; Petersson, L. Mosaic Super-resolution via Sequential Feature Pyramid Networks. In Proceedings of Proceedings of the IEEE/CVF Conference on Computer Vision and Pattern Recognition Workshops; pp. 84-85.

31. Su, T. Unsupervised evaluation-based region merging for high resolution remote sensing image segmentation. *GIScience & Remote Sensing* **2019**, *56*, 811-842.

32. Xiong, Z.; Zhang, X.; Wang, X.; Yuan, J. Self-adaptive segmentation of satellite images based on a weighted aggregation approach. *GIScience & Remote Sensing* **2019**, *56*, 233-255.

33. Wei, Y.; Zhang, K.; Ji, S. Simultaneous road surface and centerline extraction from large-scale remote sensing images using CNN-based segmentation and tracing. *IEEE Transactions on Geoscience and Remote Sensing* **2020**, *58*, 8919-8931.

34. Shamsolmoali, P.; Zareapoor, M.; Zhou, H.; Wang, R.; Yang, J. Road segmentation for remote sensing images using adversarial spatial pyramid networks. *IEEE Transactions on Geoscience and Remote Sensing* **2020**.

35. Zhang, C.; Atkinson, P.M.; George, C.; Wen, Z.; Diazgranados, M.; Gerard, F. Identifying and mapping individual plants in a highly diverse high-elevation ecosystem using UAV imagery and deep learning. *ISPRS Journal of Photogrammetry and Remote Sensing* **2020**, *169*, 280-291.

36. Li, H.; Zhang, C.; Zhang, S.; Atkinson, P.M. Crop classification from full-year fully-polarimetric L-band UAVSAR time-series using the Random Forest algorithm. *International Journal of Applied Earth Observation and Geoinformation* **2020**, *87*, 102032.

37. Tu, Y.; Chen, B.; Zhang, T.; Xu, B. Regional mapping of essential urban land use categories in China: A segmentation-based approach. *Remote Sensing* **2020**, *12*, 1058.

38. Mahata, K.; Das, R.; Das, S.; Sarkar, A. Land Use Land Cover map segmentation using Remote Sensing: A Case study of Ajoy river watershed, India. *Journal of Intelligent Systems* **2020**, *30*, 273-286.

39. Vaswani, A.; Shazeer, N.; Parmar, N.; Uszkoreit, J.; Jones, L.; Gomez, A.N.; Kaiser, Ł.; Polosukhin, I. Attention is all you need. In Proceedings of Advances in neural information processing systems; pp. 5998-6008.

40. Wang, X.; Girshick, R.; Gupta, A.; He, K. Non-local neural networks. In Proceedings of Proceedings of the IEEE conference on computer vision and pattern recognition; pp. 7794-7803.

41. Yuan, Y.; Wang, J. Ocnet: Object context network for scene parsing. *arXiv preprint arXiv:1809.00916* **2018**.

42. Zhang, H.; Zhang, H.; Wang, C.; Xie, J. Co-occurrent features in semantic segmentation. In Proceedings of Proceedings of the IEEE Conference on Computer Vision and Pattern Recognition; pp. 548-557.

43. Li, G.; Yun, I.; Kim, J.; Kim, J. Dabnet: Depth-wise asymmetric bottleneck for real-time semantic segmentation. *arXiv preprint arXiv:1907.11357* **2019**.

44. Yu, C.; Gao, C.; Wang, J.; Yu, G.; Shen, C.; Sang, N. Bisenet v2: Bilateral network with guided aggregation for real-time semantic segmentation. *arXiv preprint arXiv:2004.02147* **2020**.

45. Gu, Z.; Cheng, J.; Fu, H.; Zhou, K.; Hao, H.; Zhao, Y.; Zhang, T.; Gao, S.; Liu, J. Ce-net: Context encoder network for 2d medical image segmentation. *IEEE transactions on medical imaging* **2019**, *38*, 2281-2292.

46. Ghassemi, S.; Fiandrott, A.; Francini, G.; Magli, E. Learning and adapting robust features for satellite image segmentation on heterogeneous data sets. *IEEE Transactions on Geoscience and Remote Sensing* **2019**, *57*, 6517-6529.